RSC Advances

PAPER

View Article Online
View Journal | View Issue

Cite this: *RSC Adv.*, 2026, **16**, 501

Internal probe-external recognition immunosensor fabricated on nanochannels for reagent-free electrochemical detection of interleukin-1β

Huanrui Wang,[ab] Hongxin Wang[c] and Fei Yan *[c]

Highly sensitive and selective detection of interleukin-1β (IL-1β) enables dynamic monitoring of IL-1β levels in complex samples, providing significant clinical value for the prevention of early pathogenesis of urosepsis. Herein, a dual-functional "internal probe-external recognition" immunosensor was developed on nanochannel array, spatially separating signal generation from target recognition for label-free detection of IL-1β. A polydopamine (PDA) adhesive layer was utilized to stabilize the growth of amino-functionalized vertically-ordered mesoporous silica film (NH_2-VMSF) on a glassy carbon electrode (GCE). Using the dual functionality of NH_2-VMSF, gold nanoparticles (AuNPs) were electrochemically deposited within the NH_2-VMSF nanochannels as immobilized electrochemical probes, while antibodies were covalently immobilized on the outer surface of NH_2-VMSF to act as biological recognition elements. Upon binding with IL-1β, the immunosensor specifically recognized and captured the target, resulting in an increase in interface resistance and a corresponding decrease in the electrochemical signal of AuNPs. This mechanism enabled the quantitative analysis of IL-1β, with a linear detection range from 1 pg mL^{-1} to 100 ng mL^{-1} and a limit of detection (LOD) of 0.6 pg mL^{-1}. The immunosensor was successfully applied to IL-1β detection in fetal bovine serum (FBS). By eliminating the need for additional signal probes, the developed immunosensor simplifies the detection process, demonstrates excellent anti-interference and stability, and offers a new approach for reagent-free biomarker detection in complex samples.

Received 21st October 2025
Accepted 17th December 2025

DOI: 10.1039/d5ra08068a

rsc.li/rsc-advances

1. Introduction

Interleukin-1β (IL-1β), a principal mediator of inflammatory cascades, plays a critical role in the early pathogenesis of urosepsis.[1] This condition typically arises from severe urinary tract infections, such as acute pyelonephritis or obstruction-related infections. Upon pathogen invasion into the bloodstream, innate immune cells are activated, leading to substantial production and release of IL-1β. Once secreted, IL-1β initiates a potent downstream signalling cascade that amplifies pro-inflammatory responses, driving the clinical manifestations of systemic inflammatory response syndrome (SIRS). For instance, the concentration of IL-1β in healthy adult serum is generally maintained at a low level (<5 pg mL^{-1}) and serum IL-1β levels can rise significantly to 10–100 pg mL^{-1} or higher, during acute bacterial or viral infections (*e.g.* respiratory infections, enteritis, or tonsillitis) or acute phase of severe infections like sepsis.[2,3] Additionally, under various chronic inflammatory or tissue injury conditions, IL-1β levels show sustained elevation, commonly seen in autoimmune diseases (*e.g.*, rheumatoid arthritis), different types of hepatitis (viral or autoimmune), major trauma or postoperative injury, and within the inflammatory microenvironment associated with cancer.[4–6] Therefore, dynamic monitoring of IL-1β offers valuable insights into identifying high-risk patients likely to progress to severe sepsis or septic shock and establishing a molecular rationale for early therapeutic interventions targeting the IL-1β pathway in urosepsis.

Currently, IL-1β detection primarily relies on immunoassay techniques, including plasmon resonance[7] or fluorescent[8] methods, depending on the type of signal output. However, plasmon resonance detection is limited by its complex procedures and instrument. Although fluorescent detection offers high sensitivity, it might be affected by the original fluorescence of matrix. Electrochemical (EC) detection, with its high sensitivity, simplicity, rapid response, and ease of miniaturization, has gained significant attention in biomarker detection.[9–12] However, non-specific adsorption of proteins and other biomolecules in real samples can interfere with the accuracy and reproducibility of target detection.[13] Furthermore, immobilized probe-based reagent-free assays have emerged as an attractive approach in electrochemical biosensors.[14–16] These

[a]*Department of Urology, Peking University People's Hospital, Beijing 100044, China*
[b]*The Institute of Applied Lithotripsy Technology, Peking University, Beijing 100044, China*
[c]*School of Chemistry and Chemical Engineering, Zhejiang Sci-Tech University, Hangzhou 310018, China. E-mail: yanfei@zstu.edu.cn*

sensors immobilize signal probes on the sensing interface, eliminating the need for additional reagents, simplifying the detection process, shortening response times, and facilitating miniaturization and on-site detection.[17–19] Gold nanoparticles (AuNPs), with their excellent conductivity, high surface area, ease of functionalization, and ability to generate clear electrochemical signals, are ideal signal probes for reagent-free sensors.[20] Developing electrochemical immunosensors with anti-contamination properties and reagent-free detection is essential for the sensitive detection of IL-1β in complex biological samples.

Vertically-ordered mesoporous silica film (VMSF), with its highly ordered, vertically-oriented nanochannel structures, offers significant advantages in the construction of electrochemical biosensors due to their unique size-sieving effect, charge-selective permeability, and resistance to biofouling.[21–23] VMSF features uniform pore sizes (2–3 nm), ultra-thin film layers, and high porosity, with the internal surface of the channels rich in silanol groups ($pK_a \approx 2$–3). Due to their pore diameter being comparable to the Debye length, VMSF possess molecular-level sieving capabilities based on size, electrostatic charge, and hydrophobicity,[24–26] demonstrating great potential for electroanalysis in complex matrices. On the one hand, VMSF can effectively exclude particles and macromolecules (*e.g.* proteins, DNA) while permitting only small molecules with matching charge or hydrophobicity to diffuse through the nanochannels.[27–30] Consequently, VMSF-modified electrodes exhibit outstanding antifouling and anti-interference performance, along with the ability to selectively preconcentrate target molecules. For instance, under physiological conditions, the surface is negatively charged, effectively repelling common anionic contaminants while enabling electrostatic enrichment of target analytes, thereby enhancing detection sensitivity and selectivity.[31–33] Furthermore, the VMSF nanochannels serve as confined reactors for nanomaterials, providing an ideal environment for uniform loading and stable immobilization.[34–37] VMSF also has potential for constructing functional interface. The abundant silanol groups on the surface also offer numerous active sites for the covalent attachment of biological recognition elements, facilitating the construction of stable sensing interfaces.[38–40] Inspired by the mussel adhesion mechanism, polydopamine (PDA) can form a highly adhesive film on various substrates through oxidative self-polymerization. The catechol/amine groups in the PDA molecules can establish multiple interactions (including covalent bonds, hydrogen bonds, and π–π stacking) with the substrate and modification layers, making PDA widely used as an adhesive layer in electrode modifications.[39–41] Specifically, in the construction of VMSF-based sensors, PDA acts as a stable linking layer between VMSF and the electrode, enhancing the mechanical stability and electrochemical durability of the modified film.[42] Therefore, using PDA as an adhesive layer to stabilize the modification of VMSF on the electrode surface, coupled with the dual functionality of VMSF, allows for the confined deposition of AuNPs within the nanochannels as endogenous electrochemical probes, while antibodies are covalently immobilized on the outer surface as biological recognition elements. This design facilitates the spatial separation of signal generation and target recognition, achieving functional integration and offering advantages in reagent-free immunoanalysis.

In this work, amino-functionalized vertically-ordered mesoporous silica film (NH_2-VMSF) was stably assembled on the surface of a glassy carbon electrode (GCE) based on the interfacial adhesive effect of polydopamine (PDA). Gold nanoparticles (AuNPs) were then electrochemically deposited *in situ* within the nanochannels as endogenous electrochemical signal probes. Using glutaraldehyde as a crosslinker, IL-1β antibodies were covalently immobilized on the outer surface of NH_2-VMSF, constructing a reagent-free and anti-biofouling electrochemical immunosensor. In this design, the PDA layer ensures the strong anchoring of NH_2-VMSF on the electrode surface; NH_2-VMSF not only effectively prevents AuNPs aggregation and enhances signal stability but also has excellent anti-biofouling properties to the interface. Furthermore, AuNPs, acting as immobilized electrochemical probes, enable reagent-free detection. The sensor demonstrates good applicability in IL-1β analysis in real samples.

2. Materials and methods

2.1 Chemical and materials

Cytokines and biochemical reagents, including interleukin-1β (IL-1β), tumor necrosis factor-α (TNF-α), carcinoembryonic antigen (CEA), interferon-γ (IFN-γ), C-reactive protein (CRP), interleukin-6 (IL-6), and IL-1β-specific monoclonal antibodies, were purchased from KEY-BIO Biotechnology Co., Ltd (Beijing, China). Tetraethyl orthosilicate (TEOS, 98%), cetyltrimethylammonium bromide (CTAB), glutaraldehyde (GA), glucose, uric acid, ascorbic acid, dopamine hydrochloride, bovine serum albumin (BSA), potassium ferrocyanide (99.5%), potassium hexacyanoferrate (99.5%), sodium hydroxide (97%), sodium chloride, sodium phosphate dibasic dodecahydrate (99%), potassium chloride (99.5%), sodium dihydrogen phosphate dihydrate (99%), and sodium nitrite, were obtained from Aladdin Biochemical Technology Co., Ltd (Shanghai, China). Additionally, 3-aminopropyltriethoxysilane (APTES) and potassium hydrogen phthalate (KHP) were purchased from Macklin Biochemical Technology Co., Ltd (Shanghai, China). Phosphate-buffered saline (PBS) used in the experiments was prepared from the phosphates, and all aqueous solutions were prepared using ultrapure water (18.2 MΩ·cm).

2.2 Measurements and instrumentations

The morphology of modified electrode was characterized using a Hitachi HT7700 transmission electron microscope (TEM, Hitachi, Japan) or ULTRA 55 scanning electron microscope (SEM, Zeiss, Germany). For sample preparation, the NH_2-VMSF film was carefully scraped from the electrode surface using a blade, then dispersed in anhydrous ethanol. After ultrasonic treatment, the dispersion was drop-cast onto a copper grid and dried at room temperature. Morphological observations were conducted under an accelerating voltage of 200 kV. All electrochemical tests, including cyclic voltammetry (CV),

electrochemical impedance spectroscopy (EIS), and differential pulse voltammetry (DPV), were performed using a Metrohm PGSTAT302N electrochemical workstation (Autolab, Swiss) with a three-electrode system. The working electrode was either a bare or modified glassy carbon electrode, the reference electrode was Ag/AgCl, and the counter electrode was a platinum wire. EIS measurements were conducted over a frequency range of 0.1 Hz to 100 kHz with a perturbation amplitude of 5 mV.

2.3 Preparation of the NH_2-VMSF modified GCE

A GCE with a diameter of 3 mm was used as the supporting electrode. The electrode surface was sequentially polished with alumina powders of 0.5 μm, 0.3 μm, and 0.05 μm, followed by ultrasonic cleaning in ethanol and ultrapure water. The cleaned electrode was immersed in a Tris–HCl buffer solution (10 mM, pH 8.5) containing 2 mg per mL dopamine for 30 min to form a PDA modification layer through a self-polymerization reaction at room temperature, resulting in a PDA/GCE. Subsequently, NH_2-VMSF was grown on the PDA/GCE using an electrochemical-assisted self-assembly (EASA) method.[43] Specifically, the precursor solution was prepared by mixing 20 mL of ethanol with 20 mL of $NaNO_3$ solution, followed by the addition of CTAB (1.585 g) and APTES (0.318 mL). The pH of the mixture was adjusted to 2.97 using HCl. Subsequently, TEOS (2.732 mL) was added, and the solution was stirred at room temperature for 2.5 h. A three-electrode system was then immersed into the precursor solution. A constant potential of −2.2 V was applied to the PDA/GCE for 10 s. The electrode was then removed and thoroughly washed with ultrapure water, yielding the electrode with surfactant micelles (SM), labelled SM@NH_2-VMSF/PDA/GCE. Finally, the electrode was aged at 80 °C overnight to complete the preparation. To remove micelles, the electrode was immersed in a 0.1 M HCl–ethanol solution and stirred for 5 minutes, resulting in an NH_2-VMSF/PDA/GCE electrode with open nanochannels.

2.4 Fabrication of the immunosensor with immobilized AuNPs

The as-prepared NH_2-VMSF/PDA/GCE electrode was immersed in a 10 mM $HAuCl_4$ aqueous solution and electrodeposited at a potential of 0.5 V for 6 seconds to form AuNPs within the nanochannels, resulting in AuNPs@NH_2-VMSF/PDA/GCE. The electrode was then immersed in a glutaraldehyde (GA) solution (5%, prepared with 0.01 M PBS, pH 7.4) and reacted at 37 °C in the dark for 30 minutes. The unreacted glutaraldehyde was removed by washing with ultrapure water. Next, the obtained electrode was incubated with IL-1β antibody solution (10 μg mL^{-1}, 0.01 M PBS, pH 7.4) at 4 °C for 60 minutes. The electrode was then washed with PBS (0.01 M, pH 7.4) to remove any unbound antibodies, resulting in the formation of Ab/GA/AuNPs@NH_2-VMSF/PDA/GCE. Finally, the electrode was incubated with a 1% BSA solution at room temperature for 10 minutes to block non-specific binding sites, yielding the final immunosensor (BSA/Ab/GA/AuNPs@NH_2-VMSF/PDA/GCE).

2.5 Electrochemical detection of IL-1β

The immunosensor, BSA/Ab/GA/AuNPs@NH_2-VMSF/PDA/GCE, was incubated with IL-1β antigen solutions at different concentrations (0.01 M PBS, pH 7.4) at 4 °C for 90 minutes. After incubation, the electrode was washed with PBS (0.01 M, pH 7.4) to remove any unbound antigens. The electrochemical signals of the electrode before and after IL-1β binding were measured in 0.3 M PBS (pH 7.4) using DPV technology. The applied potential range was set from 1.2 V to 0.2 V, with an amplitude of 50 mV and a pulse width of 0.05 s. To verify the feasibility of the method for detecting IL-1β in complex samples, a standard addition method was conducted using fetal bovine serum (FBS) diluted 50 times as the sample matrix. Specifically, a known amount of IL-1β standard was spiked into the FBS samples. The spiked samples were diluted 50-fold with PBS (0.01 M, pH 7.4) before detection. The recovery (%) was obtained from the ratio of the measured concentration (found concentration) in the spiked sample to the concentration of the added standard (added concentration).

3. Results and discussion

3.1 Fabrication of the immunosensor and the mechanism for electrochemical detection of IL-1β

Fig. 1 illustrates the construction steps of the immunosensor based on immobilized AuNPs probe. In this study, GCE serves as the supporting electrode. GCE, known for its high chemical stability, wide potential window, and good biocompatibility, is one of the most commonly used electrochemical electrodes. To achieve stable modification of the VMSF on the GCE surface, a PDA adhesive layer is formed through the self-polymerization of dopamine under alkaline conditions, enhancing the stability of subsequent modifications. Next, an NH_2-VMSF was grown on the PDA/GCE using an EASA method. This process involved applying a negative voltage to induce an increase in interfacial pH, triggering the polymerization of siloxane precursors and ultimately forming a surfactant-templated ordered nanochannel structure on the electrode surface. Since APTES with amine groups was used as a co-precursor, the resulting VMSF is rich in amino groups, designated as NH_2-VMSF. After template removal using an acid-ethanol solution, open nanochannel arrays were obtained. As shown in Fig. S1 (SI), when NH_2-VMSF was grown directly on a bare GCE, a gray film could be observed covering the electrode surface. However, the edges of the NH_2-VMSF layer appeared rough, and after rinsing with ultrapure water, a large portion of the NH_2-VMSF detached, exposing the underlying GCE substrate. This indicates poor stability of NH_2-VMSF grown on bare GCE, likely due to the lack of bonding between the carbon-based electrode surface and the silica framework of NH_2-VMSF. In contrast, when NH_2-VMSF was grown on a PDA-modified GCE (PDA/GCE), a smooth-edged film was obtained. This film remained intact after rinsing with ultrapure water, which can be attributed to the strong adhesive property of the intermediate PDA layer. The enhanced adhesion originates from the oxidative self-polymerization of dopamine under alkaline conditions (typically pH > 7.5), which forms

a robust PDA film.[39] The process primarily involves: (1) oxidation of dopamine to dopamine quinone by dissolved oxygen; (2) intramolecular cyclization of dopamine quinone to yield leucodopaminechrome; (3) further oxidation and rearrangement reactions leading to the formation of key intermediates such as 5,6-dihydroxyindole and its quinone form; and (4) polymerization of these indole-based monomers through covalent and non-covalent interactions (*e.g.*, π–π stacking, hydrogen bonding), resulting in a complex cross-linked network of polydopamine. This reaction proceeds under mild conditions without requiring complex catalysts. The resulting PDA film exhibits excellent adhesion, biocompatibility, and chemical activity (rich in catechol and amine groups). Consequently, it firmly adheres to the GCE surface and can stably anchor NH_2-VMSF *via* reactions between its catechol groups and the amino groups present in NH_2-VMSF. Then, AuNPs were then electrochemically deposited within the nanochannels as endogenous electrochemical signal probes, enabling reagent-free detection. Glutaraldehyde, acting as a crosslinker, reacts with the amino groups on the NH_2-VMSF surface to introduce aldehyde groups, which covalently bind the IL-1β antibody. Finally, BSA is used to block non-specific binding sites, completing the fabrication of the immunosensor. Compared to the biotin-avidin-based oriented immobilization method, this approach offers advantages such as simplicity and low cost. Upon incubation with IL-1β, the antigen–antibody specific binding formed an immune complex, increasing the interfacial electron transfer resistance and causing a decrease in the electrochemical signal of AuNPs, thus enabling the quantitative detection of the target analyte.

3.2 Characterizations of NH_2-VMSF

The morphology and structural characteristics of NH_2-VMSF were systematically characterized using transmission electron microscopy (TEM). The TEM images clearly show that NH_2-VMSF with highly ordered nanochannel structures was successfully fabricated on the PDA-modified GCE (Fig. 2A and B). The film exhibited a uniformly distributed nanochannel array with uniform pore sizes measured to be 2–3 nm. The cross-sectional view revealed the ordered arrangement of the nanochannels, with a film thickness of approximately 109 nm.

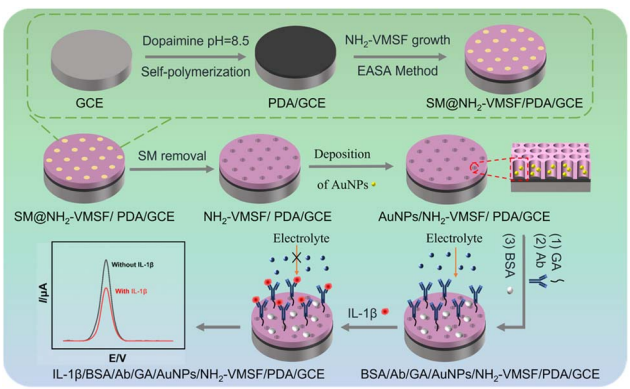

Fig. 1 Schematic of the preparation of the immunosensor based on immobilized AuNPs probe and electrochemical detection of IL-1β.

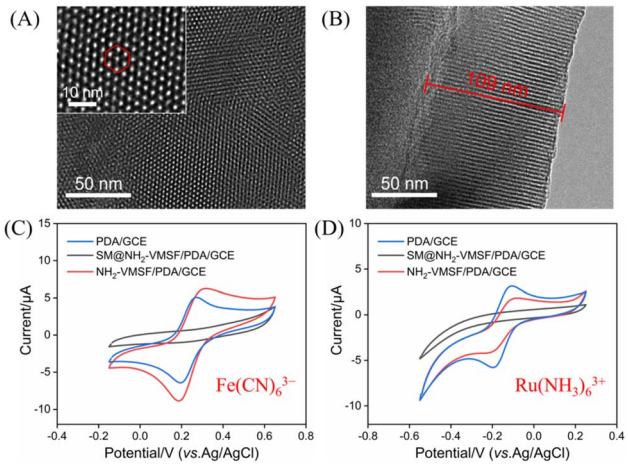

Fig. 2 (A and B) TEM planar (A) and cross-sectional (B) images of NH_2-VMSF; (C and D) CV of PDA/GCE, SM@NH_2-VMSF/PDA/GCE, and NH_2-VMSF/PDA/GCE in 0.05 M KHP solution containing 0.5 mM $Fe(CN)_6^{3-}$ (C) or $Ru(NH_3)_6^{3+}$ (D).

These nano-sized channels, smaller than the size of proteins, was important for molecular sieving effects to the NH_2-VMSF, and the regular vertical channel array facilitated fast mass transport and electron transfer.

To further investigate the charge-selective permeability and structural integrity of the functional film, cyclic voltammetry (CV) was employed with negatively charged $Fe(CN)_6^{3-}$ and positively charged $Ru(NH_3)_6^{3+}$ as electrochemical probes (Fig. 2C and D). The characterization results show that before the removal of the surfactant template, the SM@NH_2-VMSF/PDA/GCE electrode did not exhibit noticeable faradaic current responses for either of the two probes with opposite charge properties, indicating that the template micelles fully filled and effectively blocked the nanochannels, preventing the probes from contacting the electrode surface. This confirms the structural integrity and compactness of the fabricated NH_2-VMSF film. After template removal, the NH_2-VMSF/PDA/GCE showed a significant signal enhancement for the negatively charged $Fe(CN)_6^{3-}$, attributed to electrostatic attraction between the protonated amino sites in the film and the probe ions. Conversely, a significant signal suppression was observed for the positively charged $Ru(NH_3)_6^{3+}$, which was due to the electrostatic attraction between the positively charged probe and the protonated amino sites, hindering its migration within

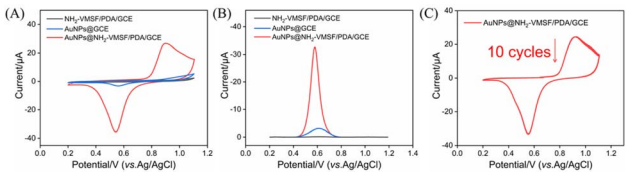

Fig. 3 CV curves (A) and DPV curves (B) of NH_2-VMSF/PDA/GCE, AuNPs@GCE, and AuNPs@NH_2-VMSF/PDA/GCE in 0.3 M PBS (pH = 7.4); (C) CV curves of AuNPs@NH_2-VMSF/PDA/GCE during consecutive scans in 0.3 M PBS (pH = 7.4).

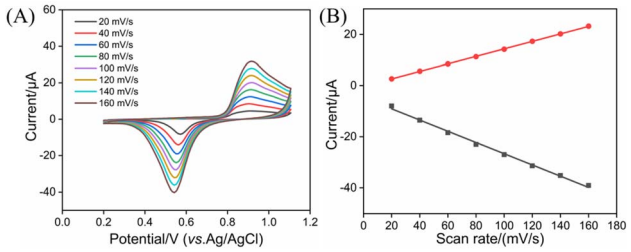

Fig. 4 (A) CV curves of AuNPs@NH_2-VMSF/PDA/GCE in 0.3 M PBS (pH = 7.4) at different scan rates. (B) Relationship between the oxidation and reduction peak currents and scan rate.

the channel. This opposing signal response behavior strongly confirmed the excellent charge-selective permeability of the NH_2-VMSF film, highlighting its potential for anti-contamination.

3.3 Characterization of AuNPs in the nanochannels

Scanning electron microscope (SEM) images of the electrode obtained on the modification process were shown in Fig. S2 (SI). It can be observed that GCE surface was relatively smooth but exhibited inherent defects such as minor cracks. After modification with PDA, a uniform wrinkled film structure was formed on its surface. Subsequently, the growth of NH_2-VMSF on this surface resulted in a smooth silica structure. Following further deposition of AuNPs, the surface morphology of the electrode showed no significant change, indicating that AuNPs were primarily deposited within the nanochannels rather than on the outer surface of NH_2-VMSF. The electrochemical behaviour of the electrode before and after AuNPs deposition was monitored using CV and DPV (Fig. 3A and B). Prior to AuNPs deposition, no noticeable redox peaks were observed for NH_2-VMSF/PDA/GCE, indicating that the supporting material itself exhibited good electrochemical inertness. After electrochemical deposition of AuNPs, a pair of distinct redox peaks appeared at approximately 0.55 V and 0.9 V, corresponding to the reduction and oxidation reactions occurring at the surface of AuNPs, respectively. This confirms that AuNPs were successfully modified onto the electrode surface and possessed good electrochemical activity. In comparison, when AuNPs were directly deposited on bare GCE, nanoparticle aggregation might occur, significantly reducing the effective surface area and resulting in much weaker electrochemical signals than those observed for AuNPs confined within NH_2-VMSF. This result clearly demonstrated that the nano-confinement effect of NH_2-VMSF effectively enhanced the electrochemical activity and interfacial electron transfer efficiency of AuNPs.

The stability of AuNPs@NH_2-VMSF/PDA/GCE was examined by performing 10 consecutive CV scans (Fig. 3C). The oxidation and reduction peak currents and potentials remained highly stable without significant attenuation, indicating that the AuNPs were strongly bound to the nanochannels and that the electrode exhibited excellent operational stability and reproducibility, suitable for multiple consecutive detections.

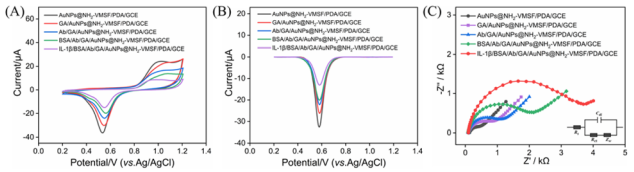

Fig. 5 The CV curves (A) and DPV curves (B) measured in 0.3 M PBS (pH = 7.4) on different electrodes obtained during the immunosensor fabrication process or after incubation of immunosensor with 1 ng/mL IL-1β. (C) EIS curves of different electrodes measured in 0.1 M KCl containing 2.5 mM $[Fe(CN)_6]^{3-/4-}$. The inset showed the corresponding equivalent circuit, including the charge transfer resistance (R_{ct}), double-layer capacitance (C_{dl}), solution resistance (R_s), and diffusion impedance (Z_w).

The influence of scan rate (ν) on the electrode reaction mechanism was further investigated (Fig. 4). The experimental results show that, within the scan rate range of 20–160 mV s^{-1}, the oxidation peak current (I_{pa}) and reduction peak current (I_{pc}) of AuNPs exhibited a good linear relationship with the scan rate ($I_{pa} = 0.146\nu - 0.275$, $R^2 = 0.999$; $I_{pc} = -0.220\nu - 4.646$, $R^2 = 0.996$), suggesting that the electrochemical reaction process was surface adsorption-controlled. This further confirmed that AuNPs were effectively confined within the vertically ordered nanochannels of NH_2-VMSF, forming a stable and controllable electrode–electrolyte interface, demonstrating highly reliable signal probes in reagent-free immunoanalysis.

3.4 Characterization of immunosensor construction and feasibility verification for IL-1β detection

The construction process of the immunosensor and its feasibility for IL-1β detection were studied using CV, DPV, and electrochemical impedance spectroscopy (EIS). As shown in Fig. 5A and B, with each modification of the electrode surface with GA, IL-1β antibody (Ab), and BSA blocking, the CV and DPV peak currents gradually decreased. This was primarily attributed to the introduction of non-conductive materials in each modification step, which weakened the interfacial electron transfer capacity, leading to a continuous decrease of the electrochemical signal. After incubating the immunosensor with the target IL-1β, the antigen–antibody specific binding

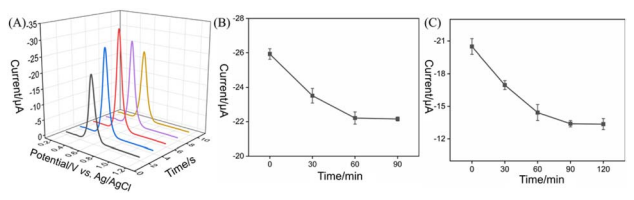

Fig. 6 DPV curves obtained on AuNPs@NH_2-VMSF/PDA/GCE prepared with different AuNPs deposition time (2, 4, 6, 8, 10 s). The electrolyte was 0.3 M PBS (pH = 7.4). (B) Effect of incubation time between IL-1β-specific antibody and GA/AuNPs@NH_2-VMSF/PDA/GCE on the current response. The concentration of IL-1β antibody was 10 μg/mL; (C) effect of incubation time between the immunosensor and IL-1β. IL-6 concentration was 1 ng/mL. Error bars represent the standard deviation of three measurements.

formed an immunocomplex that further hindered electron transfer, resulting in a significant decrease in the electrochemical signal. This confirmed that the immunosensor could achieve detection of IL-1β based on the interfacial shielding effect caused by immunorecognition.

Fig. 5C showed the corresponding EIS spectra of the electrodes obtained during the preparation process, clearly reflecting the changes in the electrode interface properties. As the modification steps progressed (from AuNPs@NH_2-VMSF/PDA/GCE through GA, Ab, and BSA modifications to final IL-1β binding), the electrode surface was progressively covered with non-conductive biomolecular layers, resulting in an increase in the charge transfer resistance at the electrode–electrolyte interface (R_{et} increased from 476 Ω to 3414 Ω). This was specifically reflected in the significant increase in the high-frequency semicircle diameter in the EIS spectra. The EIS data were fitted using the equivalent circuit model shown in the inset of Fig. 5C, yielding the R_{et} values of 476 Ω after AuNPs deposition, 1080 Ω after GA modification, 1252 Ω after Ab immobilization, 1927 Ω after BSA blocking, and 3414 Ω after IL-1β binding, respectively. The gradual increase in R_{et} was highly consistent with the changed current signals observed in CV and DPV, verifying the feasibility and reliability of the constructed immunosensor for IL-1β detection.

3.5 Optimization of immunosensor construction conditions

To enhance the detection sensitivity of IL-1β, key parameters, including the deposition time of AuNPs, antibody immobilization time, and antigen recognition time, were optimized. The effect of AuNPs deposition time on the electrochemical signal was investigated, as shown in Fig. 6A. As the deposition time increased, the DPV reduction peak current gradually increased, reaching a maximum at 6 s, followed by a decrease. The decrease in current might be attributed to excessive deposition time, which could cause nanochannel blocking, limiting the mass transfer process and reducing the redox efficiency of AuNPs on the electrode surface. Thus, 6 s was determined to be the optimal deposition time. Next, the antibody immobilization time was systematically evaluated. By monitoring the change in DPV peak current after antibody immobilization at different incubation times on the GA-activated electrode surface (Fig. 6B), it was observed that the current response gradually decreased as the incubation time increased, reflecting the increase in the amount of antibody fixed on the electrode surface. When the incubation time reached 60 min, the current change stabilized, indicating that the antibody immobilization had reached saturation. Thus, 60 min was selected as the optimal antibody immobilization time for subsequent experiments. Furthermore, the antigen incubation time was assessed by analyzing the DPV current at different incubation times (Fig. 6C), to evaluate the immunorecognition kinetics. As the incubation time increased, the current gradually decreased and plateaued at 90 min, indicating that the antigen–antibody binding reaction had reached equilibrium. Therefore, 90 min was established as the optimal incubation time for IL-1β and was used in the subsequent detection experiments.

3.6 Label-free electrochemical determination of IL-1

The performance of the constructed immunosensor for IL-1β detection was evaluated. The electrochemical signal of AuNPs was measured using DPV after the immunosensor was incubated with varying concentrations of IL-1β. As shown in Fig. 7A, the DPV peak current progressively decreased as the IL-1β concentration increased. This current reduction was attributed to the formation of an immunocomplex upon specific binding between the antigen and the immobilized antibody, which induced significant steric hindrance and interfacial resistance. These changes partially obstructed the electron transfer pathway within the nanochannels, thus decreasing the electrochemical signal from the AuNPs. Within the IL-1β concentration range of 1 pg mL^{-1} to 100 ng mL^{-1}, the peak current exhibited a good linear relationship with the logarithm of the IL-1β concentration ($\log C_{IL\text{-}1\beta}$), with the regression equation obtained as I (μA) = 2.05 $\log C_{IL\text{-}1\beta}$ (ng mL^{-1}) − 13.31 and a correlation coefficient of $R^2 = 0.998$ (Fig. 7B). The limit of detection (LOD), calculated using a signal-to-noise ratio (S/N) of 3, was determined to be 0.6 pg mL^{-1}. This LOD is lower than the concentration of IL-1β in healthy adult serum (5 pg mL^{-1}). Detection performance of IL-1β by different analytical methods were shown in Table S1 (SI).[44–50] The LOD obtained using the developed sensor was lower than that obtained using square wave voltammetry (SWV) detection based on the peptide synthesized using the YVHHYSTGQMFNGGGSC sequence/gold and silver nanoparticles immobilized on MoS_2/rGO nanosheets/reduced graphene oxide nanosheets modified gold electrode (BP1/Au-Ag@MoS_2/rGO/Au),[44] or differential pulse voltammetry (DPV) detection based on immunosensor construction by modified screen printed electrode (SPE) with BSA/Ab/chitosan/iridium oxide nanotubes/titanium carbide nanosheets (BSA/Ab /CS/IrO_X/$Ti_3C_2T_X$/SPE),[45] or fluorescent detection based on molecularly imprinted polymer/poly(ethyleneimine)/PDA/stainless steel (MIP/PEI/PDA/SS) combined with fluorescence labelled Ab (Flu-Ab)[46] or using BSA/Ab/streptavidin/the sulfosuccinimidyl-2-[biotinamido] ethyl-1,3 dithiopropionate/aminopropyltriethoxysilane/glass telecommunication fiber probe (BSA/Ab/SA/NHS-Biotin/APTES/GTF).[47] The LOD was higher than that obtained using

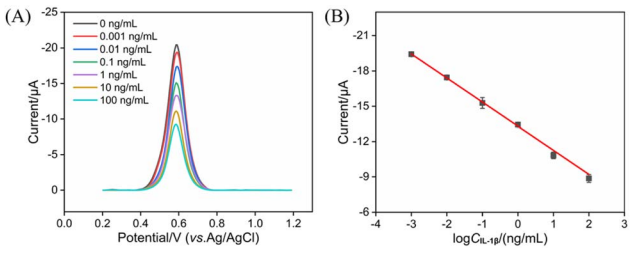

Fig. 7 (A) DPV curves of AuNPs@NH_2-VMSF/PDA/GCE prepared with different AuNPs deposition times measured in 0.3 M PBS (pH = 7.4); (B) effect of incubation time between IL-1β-specific antibody and GA/AuNPs@NH_2-VMSF/PDA/GCE on the current response. The concentration of IL-1β antibody was 10 μg /mL; (C) effect of incubation time between the immunosensor and IL-1β (1 ng/mL). Error bars represent the standard deviation of three measurements.

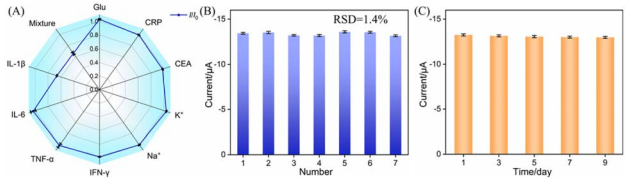

Fig. 8 (A) Selectivity and anti-interference ability of the immunosensor. The DPV cathodic peak current ratio (I/I_0) was measured before and after incubating the immunosensor with Glu (10 ng mL^{-1}), CRP (10 ng mL^{-1}), CEA (10 ng mL^{-1}), K^+ (10 ng mL^{-1}), Na^+ (10 ng mL^{-1}), IFN-γ (10 ng mL^{-1}), TNF-α (10 ng mL^{-1}), IL-6 (10 ng mL^{-1}), IL-1β (1 ng mL^{-1}), or their mixtures. (B) DPV peak currents obtained after incubating parallel-prepared immunosensors with IL-1β (1 ng mL^{-1}). (C) DPV peak currents of the developed immunosensor after storage for different days and subsequent incubation with IL-1β (1 ng mL^{-1}). Error bars i represent the standard deviation of three measurements. The test solution was 0.3 M PBS (pH = 7.4).

amperometry detection based on BSA/Ab/4-carboxyphenyl-functionalized double-walled carbon nanotubes modified screen-printed carbon electrode (BSA/Ab/HOOC-Phe-DWCNTs/SPCE),[48] or EIS detection based on BSA/Ab/*N*-(3-Dimethylaminopropyl)-*N*′-ethyl carbodiimide-NHS/6-phosphohexanoic acid modified indium tin oxide electrode (BSA/Ab/EDC-NHS/PHA/ITO)[49] or BSA/Ab/EDC-NHS/poly(2-thiophen-3-yl-malonic acid) modified ITO electrode (BSA/Ab/EDC-NHS/P3-TMA/ITO).[50] The developed sensor features simple nanomaterial synthesis and convenient electrode modification. By employing immobilized AuNPs as endogenous signal probes, it enables probe-free detection, offering advantages of easy fabrication and operational convenience.

3.7 Selectivity, anti-interference ability, reproducibility, and stability of the immunosensor

The selectivity, anti-interference ability, reproducibility, and long-term stability of the constructed immunosensor were systematically evaluated. The sensor was incubated with high concentrations of potential interfering substances commonly found in serum, including glucose, K^+, Na^+, C-reactive protein (CRP), interferon-γ (IFN-γ), interleukin-6 (IL-6), tumor necrosis factor-α (TNF-α), and carcinoembryonic antigen (CEA). The change in peak current was monitored using DPV to assess its specific recognition capability. As shown in Fig. 8A, the current responses after incubation with these interfering substances did not show any significant change compared to the initial signal, indicating that the sensor exhibits high selectivity for IL-1β. Further testing in a mixed solution containing IL-1β and various interfering substances showed a similar signal reduction to that observed with IL-1β alone, demonstrating that the sensor maintains excellent anti-interference performance and selectivity in complex matrices. Additionally, seven immunosensors were prepared in parallel for IL-1β detection. The relative standard deviation (RSD) of the detection signals from the seven electrodes was only 1.4% (Fig. 8B), confirming the excellent reproducibility in both sensor preparation and measurement. Finally, the sensor was stored at 4 °C, and its response current for IL-1β detection was measured at different time intervals. The RSD of the DPV signals from the electrodes was found to be 0.9% (Fig. 8C), indicating that the immunosensor exhibits high storage stability.

Table 1 Recoveries of IL-1β determination in spiked FBS

Analyte	Added (ng mL^{-1})	Found (ng mL^{-1})	RSD (%)	Recovery (%, n = 3)
IL-1β[a]	0.0050	0.0048	1.5	96.0
	1.00	0.942	3.8	94.2
	100	98.5	3.3	98.5

[a] The spiked FBS was diluted by a factor of 50 using PBS (0.01 M, pH 7.4). The indicated concentration of IL-1β was obtained after dilution.

3.8 Real sample analysis

To further validate the practical detection reliability of the sensing interface, the standard addition method was employed to detect IL-1β using fetal bovine serum (FBS) as a real sample matrix. Three spiked levels corresponding to physiological (healthy) and elevated (pathological) concentrations of IL-1β were tested. The recovery rates for the spiked samples ranged from 94.2% to 98.5% (Table 1), with relative standard deviations (RSD) for three replicate measurements at each concentration not exceeding 3.8%. These results demonstrate the high reliability of the immunosensor for analysis of complex biological samples. The calibration curve obtained from spiked samples (I (μA) = 2.09 log $C_{\text{IL-1β}}$ (ng/mL) − 12.98) was very close to the standard curve. This phenomenon might be attributed to the ultrasmall nanochannels of NH_2-VMSF, which can exclude biomacromolecules such as proteins *via* size exclusion effect, thereby preventing electrode fouling and contamination by proteins and consequently reducing the matrix effect. Furthermore, the sensor constructed in this work employed immobilized AuNPs as an endogenous probe, eliminating the need for an external probe during detection, which also helps reduce the influence of the matrix effect.

4. Conclusions

In summary, this work presents a reagent-free electrochemical immunosensor for IL-1β detection, based on the stable modification of NH_2-VMSF on a glassy carbon electrode surface, facilitated by a polydopamine adhesive layer. AuNPs were electrochemically deposited within the nanochannels to serve as endogenous signal probes. The ordered nanostructure of NH_2-VMSF provides both confinement effects and interface functionalization capabilities. Specifically, AuNPs were effectively immobilized within the nanochannels, ensuring high electrochemical signal stability, while the external surface was functionalized with IL-1β antibodies *via* glutaraldehyde crosslinking to form a high-specificity recognition interface. In the presence of the target, antigen–antibody binding forms an immunocomplex, increasing mass transfer resistance and resulting in a decrease in the DPV reduction peak current of

AuNPs. This enabled quantitative detection of IL-1β with wide linear range and a low limit of detection. Notably, detection was achieved without the need for an external probe, significantly simplifying the operational procedure and enhancing analytical efficiency. By integrating interface stabilization strategies, nano-confinement effects, and immobilized probe designs, this work not only facilitates highly sensitive, reagent-free IL-1β detection but also offers a versatile platform for the rapid analysis of other biomarkers in complex biological samples. In this study, GCE, commonly used carbon electrode, was employed as the supporting electrode for the sensing interface. However, GCE is relatively costly and not easily scalable or adaptable for flexible applications. Future work could explore alternative electrode materials such as screen-printed carbon electrodes, which offer lower cost and ease of mass production, enabling the development of flexible or disposable electrochemical sensing platform. Additionally, by integrating miniaturized electrochemical workstation with Bluetooth or other wireless transmission technologies, the sensing system established in this study holds potential for expansion into real-time, portable, and point-of-care testing applications, thereby offering promising for on-site analysis and personalized health monitoring.

Conflicts of interest

There are no conflicts to declare.

Data availability

The authors confirm that the data supporting the findings of this study are available within the article.

Supplementary information (SI): Table S1: detection performance of IL-1β by different analytical methods. Fig. S1: digital images of GCE (A) or PAD/GCE (B) before (left), after (middle) NH_2-VMSF growth following rinsing with ultrapure water (right). Fig. S2: SEM image of GCE (A), PDA/GCE (B), NH_2-VMSF/PDA/GCE (C) and Au NPs/NH_2-VMSF/PDA/GCE (D). See DOI: https://doi.org/10.1039/d5ra08068a.

Acknowledgements

The authors gratefully acknowledge the financial support from the National Natural Science Foundation of China (21904117) and Zhejiang Provincial Natural Science Foundation of China (LMS25B050001).

References

1 C. Rébé and F. Ghiringhelli, *Cancers*, 2020, **12**, 1791.
2 K. Khawkhiaw, J. Panaampon, T. Imemkamon and C. Saengboonmee, *World J. Gastrointest. Oncol.*, 2024, **16**, 1676–1682.
3 J. Zhang and N. Veeramachaneni, *Biomark. Res.*, 2022, **10**, 5.
4 F. Yencilek, A. Yildirim, S. G. Yilmaz, E. M. Altinkilic, A. B. Dalan, Y. Bastug and T. Isbir, *Anticancer Res.*, 2015, **35**, 6057–6061.
5 B. J. Jenkins, *The Lancet*, 2017, **390**, 1813–1814.
6 H. Wang, X. Song, Y. Wang, T. Yang, W. Liu, Y. Mou, C. Ren and X. Song, *J. Inflamm. Res.*, 2024, **17**, 9071–9085.
7 C.-Y. Chiang, M.-L. Hsieh, K.-W. Huang, L.-K. Chau, C.-M. Chang and S.-R. Lyu, *Biosens. Bioelectron.*, 2010, **26**, 1036–1042.
8 F. Deng, Y. Li, M. J. Hossain, M. D. Kendig, R. Arnold, E. M. Goldys, M. J. Morris and G. Liu, *Analyst*, 2019, **144**, 5682–5690.
9 N. Ma, X. Luo, W. Wu and J. Liu, *Nanomaterials*, 2022, **12**, 3981.
10 X. Zhu, L. Xuan, J. Gong, J. Liu, X. Wang, F. Xi and J. Chen, *Talanta*, 2022, **238**, 123027.
11 L. Yan, C. Zhang and F. Xi, *Molecules*, 2022, **27**, 5895.
12 J. Pei, X. Jia, F. Xi and B. Zhang, *Front. Chem.*, 2025, **13**, 1709420.
13 W. Hu, D. Jiang, C. Chen, Y. Zhou, S. Zhang, N. Zhang and L. Wang, *Trends Food Sci. Tech.*, 2025, **161**, 104983.
14 X. Zhou, Q. Han, J. Zhou, C. Liu and J. Liu, *Nanomaterials*, 2023, **13**, 1645.
15 J. Xing, Q. Han, J. Liu and Z. Yan, *Front. Chem.*, 2023, **11**, 1324469.
16 D. Chen, X. Luo and F. Xi, *Front. Chem.*, 2023, **11**, 1121450.
17 R. Yu, Y. Zhao and J. Liu, *Nanomaterials*, 2024, **14**, 390.
18 S. Lu, J. Wu, T. Luo, J. Liu, F. Xi and W. Zhang, *Front. Chem.*, 2024, **12**, 1493368.
19 F. Li, Q. Han and F. Xi, *Molecules*, 2023, **28**, 7867.
20 X. Wang, G. Liu, Y. Qi, Y. Yuan, J. Gao, X. Luo and T. Yang, *Anal. Chem.*, 2019, **91**, 12006–12013.
21 X. Fan, J. Wu, T. Zhang and J. Liu, *ChemBioChem*, 2024, **25**, e202400320.
22 L. Duan, C. Zhang, F. Xi, D. Su and W. Zhang, *Molecules*, 2024, **29**, 2423.
23 L. Huang, R. Su and F. Xi, *Front. Chem.*, 2023, **11**, 1126213.
24 Q. Yang, X. Lin and B. Su, *Anal. Chem.*, 2016, **88**, 10252–10258.
25 H. Ding, W. Guo, P. Zhou and B. Su, *Chem. Commun.*, 2020, **56**, 8249–8252.
26 Z. Yu, S. Zhang, J. Liu and X. Dong, *Microchem. J.*, 2026, **220**, 116599.
27 Y. Zhang, S. Zhang, J. Liu and D. Qin, *Molecules*, 2023, **28**, 6935.
28 Z. Yan, S. Zhang, J. Liu and J. Xing, *Molecules*, 2023, **28**, 5186.
29 X. Luo, T. Zhang, H. Tang and J. Liu, *Front. Nutr.*, 2022, **9**, 962736.
30 J. Gao, S. Zhang and F. Xi, *Molecules*, 2025, **30**, 746.
31 L. Zhou, H. Ding, F. Yan, W. Guo and B. Su, *Analyst*, 2018, **143**, 4756–4763.
32 J. Wu, T. Zhang, X. Jia, J. Li, H. Xie, F. Yan, D. Li and J. Liu, *J. Colloid Interface Sci.*, 2026, **701**, 138721.
33 W. Kang, J. Wu, F. Xi and H. Lai, *Microchem. J.*, 2025, **219**, 116229.
34 X. Fan, L. Wang, H. Wang, L. Huang, J. Lin, X. Gao and F. Xi, *Biosens. Bioelectron.*, 2025, **280**, 117451.
35 L. H. Ding and B. Su, *J. Electroanal. Chem.*, 2015, **736**, 83–87.
36 J. Zhao, X. Gu and J. Liu, *Microchem. J.*, 2025, **216**, 114671.

37 X. Zhou, Y. Zou, H. Ru, F. Yan and J. Liu, *Anal. Chem.*, 2024, **96**, 10264–10273.
38 X. Fan, T. Zhang, S. Wang, Y. Jiang, Y. Zhao, F. Yan and F. Xi, *Sens. Actuators, B*, 2025, **439**, 137856.
39 Z. Shi, T. Zhang, Y. Zhao, Y. Zhou and J. Liu, *Biosens. Bioelectron.*, 2025, **288**, 117828.
40 W. Zhang, Y. Jiang and F. Xi, *Anal. Chim. Acta*, 2026, **1384**, 344937.
41 H. A. Lee, Y. Ma, F. Zhou, S. Hong and H. Lee, *Acc. Chem. Res.*, 2019, **52**, 704–713.
42 X. Jin, L. Gong, J. Liang, Z. Wang, K. Wang, T. Yang and H. Zeng, *Sens. Actuators, B*, 2024, **407**, 135485.
43 A. Walcarius, E. Sibottier, M. Etienne and J. Ghanbaja, *Nat. Mater.*, 2007, **6**, 602–608.
44 H. J. Yang, C. V. Raju, C.-H. Choi and J. P. Park, *Anal. Chim. Acta*, 2024, **1295**, 342287.
45 W. Zhang, J. Du, K. Wang, Y. Li, C. Chen, L. Yang, Z. Kan, B. Dong, L. Wang and L. Xu, *Anal. Chim. Acta*, 2023, **1247**, 340878.
46 F. Deng, E. M. Goldys and G. Liu, *Sens. Actuators, B*, 2019, **292**, 277–283.
47 K. Zhang, A. Arman, A. G. Anwer, M. R. Hutchinson and E. M. Goldys, *Sens. Actuators, B*, 2019, **282**, 122–129.
48 E. B. Aydın and M. K. Sezgintürk, *Anal. Chim. Acta*, 2018, **1039**, 41–50.
49 E. Sánchez-Tirado, C. Salvo, A. González-Cortés, P. Yáñez-Sedeño, F. Langa and J. M. Pingarrón, *Anal. Chim. Acta*, 2017, **959**, 66–73.
50 E. B. Aydın, M. Aydın and M. K. Sezgintürk, *Sens. Actuators, B*, 2018, **270**, 18–27.